



Water vapour lidar
calibration

A. Foth et al.

This discussion paper is/has been under review for the journal Atmospheric Chemistry and Physics (ACP). Please refer to the corresponding final paper in ACP if available.

Water vapour profiles from Raman lidar automatically calibrated by microwave radiometer data during HOPE

A. Foth¹, H. Baars², P. Di Girolamo³, and B. Pospichal¹

¹Leipzig Institute for Meteorology, University of Leipzig, Leipzig, Germany

²Leibniz Institute for Tropospheric Research, Leipzig, Germany

³Scuola di Ingegneria, Università degli Studi della Basilicata, Potenza, Italy

Received: 8 December 2014 – Accepted: 13 February 2015 – Published: 5 March 2015

Correspondence to: A. Foth (andreas.foth@uni-leipzig.de)

Published by Copernicus Publications on behalf of the European Geosciences Union.

Title Page

Abstract

Introduction

Conclusions

References

Tables

Figures



Back

Close

Full Screen / Esc

Printer-friendly Version

Interactive Discussion



Abstract

In this paper, we present a method to derive water vapour profiles from Raman lidar measurements calibrated by the integrated water vapour (IWV) from a collocated microwave radiometer during the intense observation campaign HOPE in the frame of the HD(CP)² initiative. The simultaneous observation of a microwave radiometer and a Raman lidar allowed an operational and continuous measurement of water vapour profiles also during cloudy conditions. The calibration method provides results in a good agreement with conventional methods based on radiosondes. The calibration factor derived from the proposed IWV method is very stable with a relative uncertainty of 6%. This stability allows to calibrate the lidar even in the presence of clouds using the calibration factor determined during the closest in time clear sky interval. Based on the application of this approach, it is possible to retrieve water vapour profiles during all non-precipitating conditions. A statistical analysis shows a good agreement between the lidar measurements and collocated radiosondes. The relative biases amount to less than 6.7 % below 2 km.

1 Introduction

Water vapour plays a key role in the description of the thermodynamic state of the atmosphere (Hartmann et al., 2013) and it is the most important greenhouse gas (Twomey, 1991). Its amount in the atmosphere is controlled mostly by the air temperature, rather than by emissions. Therefore, tropospheric water vapour is considered as a feedback agent more than a forcing to climate change. Due to its spatio-temporal variability and its involvement in many atmospheric processes (e.g. cloud formation) it is difficult to properly implement water vapour in climate models (Held and Soden, 2000; Tompkins, 2002). Uncertainties in both observations and modelling of water vapour strongly affect the representation of clouds and precipitation in climate models and predictions. For that reason the German research project High Definition Clouds and Precipitation for

ACPD

15, 6567–6599, 2015

Water vapour lidar calibration

A. Foth et al.

Title Page

Abstract

Introduction

Conclusions

References

Tables

Figures



Back

Close

Full Screen / Esc

Printer-friendly Version

Interactive Discussion



Water vapour lidar calibration

A. Foth et al.

Title Page

Abstract

Introduction

Conclusions

References

Tables

Figures



Back

Close

Full Screen / Esc

Printer-friendly Version

Interactive Discussion



advancing Climate Prediction (HD(CP)²) was initiated aiming to improve the clouds and precipitation representation in models and to quantify the errors associated. One part within the HD(CP)² initiative was the intense observation campaign HD(CP)² Observational Prototype Experiment (HOPE) in Jülich. During HOPE different remote sensing instruments to measure water vapour, both active and passive, were deployed. An active method is given by the Raman lidar technique (Ansmann et al., 1992; Whiteman et al., 1992; Wandinger, 2005). Raman lidars enable high vertical resolution measurements of water vapour and were therefore applied in several field studies such as IHOP (Weckwerth et al., 2004; Whiteman et al., 2006b) or COPS (Herold et al., 2011; Wulfmeyer et al., 2011; Bhawar et al., 2011). However, Raman lidars provide no water vapour information from inside the cloud or above (for optically thick clouds) so that lidar measurements are limited from the surface to the cloud base. Furthermore, daytime measurements are limited in height due to the presence of scattered solar radiation. In addition, water vapour Raman lidars need to be calibrated with an instrument measuring simultaneously for example a microwave radiometer (MWR) or radiosonde (RS) (Madonna et al., 2011; Mattis et al., 2002).

Passive microwave radiometry provides atmospheric water vapour observations with high temporal resolution, but limited vertical information (Westwater et al., 2005). However, the integrated water vapour (IWV) can be retrieved very accurately. In addition, microwave radiometers can be operated during all weather conditions except for precipitation.

In contrast to the already presented remote sensing observations water vapour profiles can be measured in-situ using radiosondes. RS launches are mostly performed by the national weather services and usually twice a day. Therefore, the horizontal and temporal resolution of routine measurements is rather low.

As described above it is a challenge to provide continuous high-resolution water vapour profiles with a single instrument. In recent years several supersites, like the Jülich Observatory for Cloud Evolution (JOYCE), the Leipzig Aerosol and Cloud Remote Observations System (LACROS) and the Richard Assmann Observatory (RAO),

Water vapour lidar calibration

A. Foth et al.

Title Page

Abstract

Introduction

Conclusions

References

Tables

Figures



Back

Close

Full Screen / Esc

Printer-friendly Version

Interactive Discussion



installed a combination of remote sensing systems. The synergy of these instruments provides complementary information on the water vapour structure. Thus, when both Raman lidar and MWR are measuring collocated and simultaneously at the supersites, continuous water vapour profiles can be obtained operationally. The major objective of this paper is to apply a calibration method which is only based on IWV from MWR in a very straightforward way to offer a broad application. In previous approaches the total precipitable water from MWR in combination with RS has been used to calibrate the water vapour Raman lidar (Turner and Goldsmith, 1999; Turner et al., 2002). We demonstrate that the lidar calibration with MWR is as accurate as conventional methods based on RS allowing operational applicability.

2 Instrumentation

In the framework of the HD(CP)² initiative HOPE was conducted around Jülich in western Germany during April and May 2013 (Macke, 2014). The goal of HOPE was to probe the atmosphere with a specific focus on the development of clouds and precipitation. HOPE was further conceived for a critical model evaluation and to provide information on sub-grid variability and microphysical properties. Two observatories were set up in addition to JOYCE. The LACROS site was temporarily built up in Krauthausen which is about 4 km south of JOYCE. Both JOYCE and LACROS observatories dispose of a set of active and passive remote sensing instruments such as lidars and MWRs. Radiosondes were launched in Hambach which is about 4 km away from JOYCE and LACROS. In the following subsections we present the instruments used for this study.

2.1 Lidars

2.1.1 Polly^{XT}

The lidar measurements at the LACROS site were conducted with the fully automatic portable multiwavelengths Raman and polarization lidar Polly^{XT} (Althausen et al.,

focussed on demonstrating the automated calibration procedure. This in order to simplify the data analysis procedure and allow an easier implementation of the automated calibration procedure.

2.2 Microwave radiometer HATPRO

5 The MWR is a passive instrument that measures atmospheric emission at two frequency bands in the microwave spectrum. Seven channels are along the 22.235 GHz H₂O absorption line. From these observations humidity informations can be retrieved. The seven channels of the other band from 51 to 58 GHz along the O₂ absorption complex contain the vertical temperature profile information. The fully automatic microwave radiometer HATPRO allows to derive temperature and humidity profiles as well as integrated quantities such as IWV and liquid water path (LWP) with a high temporal resolution up to 1 s (Rose et al., 2005). Observations are possible during nearly all weather conditions except for precipitation.

10 To retrieve atmospheric quantities from the measured brightness temperatures, statistical algorithms were used by means of a multi-linear regression between modelled brightness temperatures and atmospheric profiles. Both MWRs from JOYCE and LACROS use the same retrieval algorithms which are based on a long-term dataset of De Bilt radiosondes (Löhnert and Crewell, 2003). The accuracy of the temperature information in the planetary boundary layer can be enhanced through measurements at different elevation angles (Crewell and Löhnert, 2007). The scan mode requires horizontally homogeneous atmospheric conditions in the direct horizontal vicinity (~ 3 km).

2.3 Radiosonde

15 Radiosondes (RS) were launched minimum twice a day (11:00 and 23:00 UTC) and more often during intensive observation periods (IOP) at the KITCube site in Hambach. The RS (type Graw DFM-09) measures temperature, humidity, pressure and wind velocity (Nash et al., 2011). Due to the vicinity of the RS station to the open-cast mining

Water vapour lidar calibration

A. Foth et al.

Title Page

Abstract

Introduction

Conclusions

References

Tables

Figures



Back

Close

Full Screen / Esc

Printer-friendly Version

Interactive Discussion



and its depth of nearly 400 m, horizontal inhomogeneities between the RS and the lidar locations are likely (Fig. 1).

3 Methodology

The Raman lidar technique enables the determination of water vapour mixing ratio profiles using the inelastic backscatter from nitrogen at 387 nm and from water vapour at 407 nm (Whiteman, 2003; Wandinger, 2005). The Raman lidar equation for inelastic signals can be written as

$$P_{\lambda_R}(z) = \frac{K O_{\lambda_R}(z)}{z^2} \beta_{\lambda_R}(z) \times \exp \left\{ - \int_0^z [\alpha_{\lambda_0}(\xi) + \alpha_{\lambda_R}(\xi)] d\xi \right\} \quad (1)$$

and describes the Raman signals $P_{\lambda_R}(z)$ from distance z measured with lidar at the Raman wavelength λ_R . K is the system constant and combines all the range-independent system parameters. $O_{\lambda_R}(z)$ is the overlap factor. $\beta_{\lambda_R}(z)$ denotes the molecular backscatter coefficient as a function of range. The exponential term characterises the extinction of light on the way from the lidar to the backscattering molecule ($\alpha_{\lambda_0}(z)$) at the emitted wavelength λ_0 and on the way back to the lidar ($\alpha_{\lambda_R}(z)$) at the Raman wavelength λ_R . One has to consider that the wavelength is shifted after the Raman scattering process.

The Raman backscatter coefficient

$$\beta_{\lambda_R}(z) = N_{\lambda_R}(z) \frac{d\sigma_{\lambda_R}(\pi)}{d\Omega} \quad (2)$$

is given by the molecule number density $N_{\lambda_R}(z)$ of the Raman-active gas and the differential cross section for the backward direction $d\sigma_{\lambda_R}(\pi)/d\Omega$. Based on Eqs. (1) and (2) the mixing-ratio of water vapour to dry air $m_{\text{H}_2\text{O}}$ is determined by forming the ratio of



the lidar returns from water vapour and molecular nitrogen:

$$m_{\text{H}_2\text{O}} = C_{\text{H}_2\text{O}} \frac{P_{\text{H}_2\text{O}}(z)}{P_{\text{N}_2}(z)} \frac{\exp\left[-\int_0^z \alpha_{\lambda_{\text{N}_2}}(\xi) d(\xi)\right]}{\exp\left[-\int_0^z \alpha_{\lambda_{\text{H}_2\text{O}}}(\xi) d(\xi)\right]}. \quad (3)$$

In Eq. (3) identical overlap factors were assumed. Differences in the range-independent Raman backscatter cross sections for both channels are adsorbed within the calibration factor $C_{\text{H}_2\text{O}}$ whereon we focus in this paper. The second term indicates the signal ratio which is directly measured. The third term describes the difference between the atmospheric transmission at λ_{N_2} and $\lambda_{\text{H}_2\text{O}}$. The extinction coefficients $\alpha_{\lambda_{\text{N}_2}}(z)$ and $\alpha_{\lambda_{\text{H}_2\text{O}}}(z)$ consist of a molecular (superscript m) and a particle part (superscript p). Figure 2a and b displays the vertical profiles of the molecular and particle extinction coefficients for both Raman channels on 5 May 2013, 23:10 UTC measured with Polly^{XT}. $\alpha_{\lambda_{\text{N}_2}}^m(z)$ and $\alpha_{\lambda_{\text{H}_2\text{O}}}^m(z)$ are calculated by using temperature profiles from the MWR and standard atmosphere pressure profiles (Bucholtz, 1995). $\alpha_{\lambda_{\text{N}_2}}^p(z)$ and $\alpha_{\lambda_{\text{H}_2\text{O}}}^p(z)$ can be determined by the Raman method using the particle extinction coefficient at 355 nm and a certain Ångström-exponent, but they are strongly influenced by the overlap effect. In contrast, the particle backscatter coefficient from the Raman method is a ratio product from the elastic signal at 355 nm and the inelastic signal at 387 nm and, therefore, it is not affected by the overlap (Ansmann et al., 1992). Hence, the particle extinction coefficients are calculated from the particle backscatter coefficients multiplied by a certain height-independent lidar ratio (i.e. extinction-to-backscatter ratio) of 50 sr (Müller et al., 2007) to receive more reliable values below 1 km. The particle extinction coefficients are strongly smoothed, therefore, there is no strong decrease in the lowermost layers. For the calculation of the particle backscatter coefficient at the Raman wavelengths, a spectral dependence with a backscatter-related Ångström-exponent of 1 is assumed. The determined aerosol optical depth (AOD) at 355 nm amounts to 0.22 on 5 May 2013, 23:10 UTC.

Water vapour lidar calibration

A. Foth et al.

Title Page

Abstract

Introduction

Conclusions

References

Tables

Figures



Back

Close

Full Screen / Esc

Printer-friendly Version

Interactive Discussion



Water vapour lidar calibration

A. Foth et al.

Title Page

Abstract

Introduction

Conclusions

References

Tables

Figures



Back

Close

Full Screen / Esc

Printer-friendly Version

Interactive Discussion



The resulting differential transmission ratios are illustrated in Fig. 2c. The black line indicates the influence by the differences in the atmospheric transmission at both Raman wavelengths. With a longer path through the atmosphere the influence of the differential transmission increases. By completely neglecting the differences in the atmospheric transmission, the error is less than 2.9% below 2 km where most of the water vapour is located. In 10 km the value is 6.8% but in this altitude the amount of water vapour is rather low. Since it is quite an effort to retrieve aerosol extinction profiles operationally, we neglect the particle contribution to the transmission. The resulting error amounts to 1.3% at 2 km (blue line). These values are in a good agreement with studies on a modelled atmosphere (Whiteman, 2003).

The temperature dependence of the water vapour Raman spectrum portion that is selected by the interference filter is not considered in this paper. For the optical setup of both lidars used here, the effect is negligible in the lower troposphere according to Whiteman (2003).

For Polly^{XT} and BASIL the lowermost 400 and 100 m, respectively, of the signal ratio are assumed to be well mixed and are set constant to account for the overlap problem.

3.1 Calibration methods

After considering the uncertainties explained above, the calibration factor $C_{\text{H}_2\text{O}}$ can be determined by comparison with simultaneous measurements from a reference instrument. In the following subsections three different methods with two instruments (MWR and RS) are presented in detail for a clear sky night from a Polly^{XT} measurement on 5 May 2013 (HOPE IOP 12). Afterwards, the stability of the IWV method during the two month period of HOPE is presented.

3.1.1 Regression method

The regression method can be used to calibrate the lidar profile with a RS (England et al., 1992). Therefore, a linear regression between the water vapour mixing ratio from

Water vapour lidar calibration

A. Foth et al.

Title Page

Abstract

Introduction

Conclusions

References

Tables

Figures



Back

Close

Full Screen / Esc

Printer-friendly Version

Interactive Discussion



the RS and the signal ratio $P_{\text{H}_2\text{O}}/P_{\text{N}_2}$ from the lidar is performed (see Fig. 3a). The calibration factor $C_{\text{H}_2\text{O}}$ is defined as the slope of the regression line. In our case, the calibration factor amounts to 12.15 g kg^{-1} . The standard error of the slope ($\sigma C_{\text{H}_2\text{O}}$) is 0.21 g kg^{-1} and the correlation coefficient $R^2 = 0.98$ shows a good correlation between the lidar signal and the mixing ratio from the RS. This results in a relative error of 1.7%. The signal ratio is corrected for differential transmission and is averaged over 20 min from 23:00 to 23:20 UTC. The vertical smoothing amounts to 270 m. Only an altitude region from 2 up to 5 km is regarded for the regression to exclude boundary layer inhomogeneities in the water vapour structure and to avoid differences due to the RS drift in higher altitudes. Using this method, Dionisi et al. (2010) found a variability in the calibration factor of about 10%.

3.1.2 Profile method

Another method to calibrate the lidar with a RS is the profile method with an associated uncertainty of about 5% (Mattis et al., 2002; Reichardt et al., 2012). $C_{\text{H}_2\text{O}}$ is calculated by the temporal mean of the water vapour mixing ratio measured with RS and the signal ratio from the lidar for each considered height bin. This ratio varies with altitude resulting in a mean calibration factor of 12.56 g kg^{-1} and a standard deviation of 1.12 g kg^{-1} (Fig. 3b). The relative error amounts to 9%. Here, the same time range, altitude region and vertical smoothing as for the regression method are applied.

3.1.3 IWV method

In previous experiments (Ferrare et al., 1995; Herold et al., 2011), radiosondes showed a significant sonde-to-sonde variability (Nash et al., 2005) as well as a dry bias (Turner et al., 2003). For that reason, water vapour Raman lidars were often calibrated based on the IWV retrieved from a MWR resulting in a relative uncertainty of 5% (Turner and Goldsmith, 1999) and 7% (Madonna et al., 2011), respectively.

Water vapour lidar calibration

A. Foth et al.

Title Page

Abstract

Introduction

Conclusions

References

Tables

Figures

◀

▶

◀

▶

Back

Close

Full Screen / Esc

Printer-friendly Version

Interactive Discussion



Before using the MWR for the calibration of the lidar it is necessary to estimate the error of the IWV. Figure 4 displays the IWV comparison between MWR and RS. On average the bias during all weather conditions and clear sky is very low with values of -0.01 ± 0.96 and $0.02 \pm 0.92 \text{ kg m}^{-2}$ (mean \pm SD), respectively. However, during drier (IWV $< 7 \text{ kg m}^{-2}$) or more humid (IWV $> 20 \text{ kg m}^{-2}$) clear sky conditions the relative difference can amount up to 10 %. These relative differences have to be considered when calibrating lidar profiles.

Using the IWV method, $C_{\text{H}_2\text{O}}$ is defined as the ratio of the IWV measured with the MWR and the integrated signal ratio from the lidar. For simultaneous measurements from MWR and lidar, $C_{\text{H}_2\text{O}}$ can be calculated from the mean of its time series during clear sky. To determine clear sky periods, two criteria are used. First, the standard-deviation of LWP from MWR within a 20 min interval should amount to less than a threshold of 1.5 g m^{-2} . The second one is based on the detection of a potential cloud base with the lidar signal at 1064 nm. Profiles with cloud bases higher than 6 km are treated as clear sky profiles. For that reason, the integrated signal ratio of the lidar is calculated by integrating the profiles from ground to 6 km. Water vapour above this height is mostly negligible. In that way, the lidar can be calibrated in the presence of high clouds.

The time series of the calculated $C_{\text{H}_2\text{O}}$ is presented in Fig. 3c. The mean and the standard deviation are 12.77 and 0.36 g kg^{-1} , respectively. Regarding only the time range which is used for the calibration with the RS, the mean amounts to 12.78 g kg^{-1} and the standard deviation to 0.3 g kg^{-1} . The relative error does thus not exceed 3 %.

To give an overview, the calibration factors and errors of all presented methods are summarized in Table 1. The relative difference between these method amounts to less than 5 %. The IWV method is well suited to avoid errors due to the RS drift.

3.2 Stability of the calibration factor

Having demonstrated that the calibration factors of all the three methods are in a good agreement, we will here discuss the stability of the IWV method. Figure 5 presents the time series of the calibration factor of Polly^{XT} using the IWV method. Rearrangements in the optical setup of Polly^{XT} specifically modifications on the grey filters are indicated by grey dashed lines. The means and standard deviations amount to $15.7 \pm 1.0 \text{ g kg}^{-1}$ and $12.5 \pm 0.6 \text{ g kg}^{-1}$ before and after the rearrangement in the optical setup, respectively. These values correspond to relative errors of 6 and 5 % and are comparable to studies of Mona et al. (2007) and Sakai et al. (2007). Without any strong rearrangements in the optical setup, the calibration factor is very stable, enabling an operational applicability. This is particularly important during cloudy conditions when no calibration can be performed. In those cases, the calibration factor from the last 20 min clear sky interval can be applied. This is explained in more detail in Sect. 4.4.

4 Water vapour measurements

The availability of two Raman lidar systems as well as frequent RS launches allow a statistical analysis of the water vapour profile accuracy. This section starts with an overview over the Polly^{XT} water vapour observation during HOPE. Afterwards, a case study comparing water vapour measurements of Polly^{XT}, BASIL and RS is presented. This part is followed by an extensive statistical analysis showing the accuracy of the IWV method for the whole experimental period in Western Germany. Finally, this section ends with an example of a water vapour measurement in the presence of clouds.

4.1 Overview over Polly^{XT} water vapour observations during HOPE

Using the IWV method, it was possible to obtain calibrated water vapour profiles by Polly^{XT} during almost every night from 4 April to 29 May 2013 (Fig. 6). The water vapour content in the planetary boundary layer (PBL) is quite variable ranging from

about 3 g kg^{-1} on 7 April up to about 8 g kg^{-1} on 8 May 2013. The PBL contains more water vapour than the layers above. However, the water vapour in the top layers was often not observed due the presence of clouds (e.g. night from 11 to 12 April 2013). A method to derive water vapour also in cloudy cases is presented in Sect. 4.4.

4.2 Comparison of water vapour measurements on 5 May 2013

During a night of 5 to 6 May 2013, clear sky conditions were present over the area and all measurement systems were running. Figure 7a shows a comparison of water vapour mixing ratio profiles from Polly^{XT}, BASIL and RS at 23:00 UTC. The lidar profiles are averaged over 20 min starting at 23:00 UTC. The vertical smoothing lengths are 90 and 22.5 m for Polly^{XT} and BASIL, respectively. Due to the different vertical resolution, the lidar profiles are interpolated to the RS height grid. All three curves are in a good agreement, except within the PBL up to 1.6 km. Above the PBL top a strong decrease in the water vapour mixing ratio could be observed. The differences between the RS as independent reference and the lidars are illustrated in Fig. 7b. It can be seen that the differences are quite large in the PBL. The mean difference and its standard deviation in the PBL amount to $-0.31 \pm 0.29 \text{ g kg}^{-1}$ (relative error $-6.6 \pm 7.1 \%$) and $-0.37 \pm 0.44 \text{ g kg}^{-1}$ ($-8.3 \pm 10.2 \%$) for Polly^{XT} (black) and BASIL (red), respectively. These differences are expected due to the normal water vapour variability in the PBL. Negative values indicate drier RS values.

The largest differences occur at the PBL top down to -1 g kg^{-1} (Polly^{XT}) and -1.37 g kg^{-1} (BASIL) which can be caused by small-scale variability of the PBL height. Above the PBL in the free troposphere (FT) between 2 and 5 km the differences are smaller with values of $0.13 \pm 0.16 \text{ g kg}^{-1}$ ($7.4 \pm 10.3 \%$) for Polly^{XT} and $0.07 \pm 0.12 \text{ g kg}^{-1}$ ($2.8 \pm 9.1 \%$) for BASIL.

Title Page

Abstract

Introduction

Conclusions

References

Tables

Figures



Back

Close

Full Screen / Esc

Printer-friendly Version

Interactive Discussion



4.3 Statistical analysis

For a statistical analysis of the absolute bias between RS and Polly^{XT} and between RS and BASIL only clear sky nighttime measurements within less than 2 h before or after the RS launch time are considered. The sample size amounts to 66 and 33 observations, respectively. The profiles are interpolated to the height grid of the lidar and are averaged over 20 min. For the comparison between both lidars only simultaneous 20 min averages are investigated (19 cases). One has to consider that several lidar profiles were compared to one RS profile (e.g. lidar profiles from 21:20, 21:40 and 22:00 UTC to the RS from 23:00 UTC).

The absolute bias between RS and Polly^{XT}, as well as the absolute bias between RS and BASIL are largest in the lowermost layer from 0 to 0.5 km (Fig. 8a). These biases are induced by the different measurement locations and the missing gluing in the BASIL data. This can have an impact on the mixing ratio of up to 1 g kg^{-1} in the lowermost 500 m. In the PBL up to about 2 km, the absolute bias between RS and BASIL and between Polly^{XT} and BASIL shows negative values indicating that BASIL measures a higher amount of water vapour. These higher biases in the PBL can be explained by the higher variability of water vapour due to the different measurement locations, since the RS launch site (KIT) is directly situated at the open-cast mining.

The trajectories of the RS up to an altitude of 2 km are shown in Fig. 1 split into the trajectories west and east. Figure 9 depicts the biases between RS and Polly^{XT} distinguished by the direction of the RS trajectories. When the RS drifts to the east (red), the RS rises in an air mass which is not affected by the pit. In these cases, the bias is close to zero at altitudes from 0.5 to 1 km. During the weaker easterly wind conditions, the RS drifts in an air mass which is strongly affected by the pit, whereas the air sounded by the lidar passes the pit southwards and is therefore not disturbed. Here the lidar and the RS do not profile the same air masses resulting in a higher bias down to -0.3 g kg^{-1} .

Title Page

Abstract

Introduction

Conclusions

References

Tables

Figures



Back

Close

Full Screen / Esc

Printer-friendly Version

Interactive Discussion



Water vapour lidar calibration

A. Foth et al.

Title Page

Abstract

Introduction

Conclusions

References

Tables

Figures



Back

Close

Full Screen / Esc

Printer-friendly Version

Interactive Discussion



Above the PBL the biases converge to zero (Fig. 8a). The bias between the RS and Polly^{XT} shows a small increase at about 2.5 km caused by 4 cases in which the atmosphere changes so fast that the lidar and the RS do not measure the same air mass. In high altitudes no significant biases are noticeable. Obviously, the water vapour amount decreases with altitude and therefore the RMSE also decrease with height (Fig. 8b). The coefficient of variation (CV) also known as relative RMSE increases with height due to the less water vapour amount (Fig. 8c). In high altitudes the CV is more noisy for all three comparisons.

The bias of the previously described comparisons is summarised in Table 2. It can be seen that the absolute bias is larger in the lower layers up to 4 km than in the upper layer (4 to 10 km). However, large relative biases can occur in the upper layer due to the lower water vapour mixing ratio. Brocard et al. (2013) found relative biases within 3% up to 3 km during the day, and within 5 to 10% up to 8 km during the night. Values of about $0.6 \pm 0.6 \text{ g kg}^{-1}$ in the altitude range 1.5 to 5.5 km were identified by Navas-Guzmán et al. (2014).

4.4 Water vapour measurements below clouds

After showing the stability and accuracy of the calibration factor from the IWV method we can calibrate the lidar profiles during all non-precipitating conditions. Figure 10a shows the height-time display of the water vapour mixing ratio from a Polly^{XT} measurement on 16 April 2013, 00:40 UTC. The white area indicates regions inside or above clouds without any water vapour information. The cloud base was determined by the gradient method on the range-corrected signal at 1064 nm (Baars et al., 2008). The green marked profiles until 01:20 UTC are calibrated with the IWV method, whereas the red marked after 01:20 UTC indicate cloudy conditions. These profiles are calibrated using the averaged calibration factor of the last 20 min clear sky interval (01:00 to 01:20 UTC). Both profiles of the water vapour mixing ratio at 01:00 and 02:20 UTC are in a good agreement below the cloud base (Fig. 10b). With this technique it is

possible to provide continuous water vapour profiles up to the cloud base in all non-precipitating night cases.

5 Conclusions

In this study, we present water vapour profiles from Raman lidar automatically calibrated by microwave radiometer enabling an operational applicability. It is shown that the calibration factors during HOPE were very stable with a relative error of 6%. This allowed us to retrieve water vapour profiles in all non-precipitating weather condition. During clear sky cases, the lidar can be calibrated simultaneously with the IWV from the MWR, whereas in cloudy cases the calibration factor from the last 20 min clear sky interval can be applied. Therefore, the lidar setup should only be changed during clear sky conditions.

The presented case study and the statistical analysis show a good agreement between measurements with RS and two different lidar systems calibrated by MWR. This results in rather accurate profiles. The biases between the lidars and the RS can be explained by the different measurement locations and a possible systematic bias in the RS. This could be investigated in further studies.

Finally, we showed the ability of the systems to measure continuous water vapour profiles in cloudy cases from ground up to cloud base. To retrieve water vapour information from within and above the cloud we will develop a two-step algorithm combining the Raman lidar mass mixing ratio and MWR brightness temperatures. Both steps, the Kalman filter and the one dimensional-variational retrieval method will improve the accuracy of the water vapour measurement and will provide reliable data under most conditions except during rainy periods.

Acknowledgements. This work was funded by the Federal Ministry of Education and Research in Germany (BMBF) through the research programme “High Definition Clouds and Precipitation for Climate Prediction – HD(CP)²” (FKZ: 01LK1209D).

Water vapour lidar calibration

A. Foth et al.

Title Page

Abstract

Introduction

Conclusions

References

Tables

Figures



Back

Close

Full Screen / Esc

Printer-friendly Version

Interactive Discussion



The authors acknowledge the BASIL, the LACROS and the radiosonde team for conducting the measurements and like to acknowledge all other supporters of the HOPE campaign.

References

- Althausen, D., Engelmann, R., Baars, H., Heese, B., Ansmann, A., Müller, D., and Komppula, M.: Portable Raman lidar Polly^{XT} for automated profiling of aerosol backscatter, extinction, and depolarization, *J. Atmos. Ocean. Tech.*, 26, 2366–2378, doi:10.1175/2009JTECHA1304.1, 2009. 6570
- Ansmann, A., Wandinger, U., Riebesell, M., Weitkamp, C., and Michaelis, W.: Independent measurement of extinction and backscatter profiles in cirrus clouds by using a combined Raman elastic-backscatter lidar, *Appl. Optics*, 31, 7113–7131, doi:10.1364/AO.31.007113, 1992. 6569, 6574
- Baars, H., Ansmann, A., Engelmann, R., and Althausen, D.: Continuous monitoring of the boundary-layer top with lidar, *Atmos. Chem. Phys.*, 8, 7281–7296, doi:10.5194/acp-8-7281-2008, 2008. 6581
- Bhavar, R., di Girolamo, P., Summa, D., Flamant, C., Althausen, D., Behrendt, A., Kiemle, C., Bossler, P., Cacciani, M., Champollion, C., di Iorio, T., Engelmann, R., Herold, C., Müller, D., Pal, S., Wirth, M., and Wulfmeyer, V.: The water vapour intercomparison effort in the framework of the convective and orographically-induced precipitation study: airborne-to-ground-based and airborne-to-airborne lidar systems, *Q. J. Roy. Meteor. Soc.*, 137, 325–348, doi:10.1002/qj.697, 2011. 6569
- Brocard, E., Philipona, R., Haeferle, A., Romanens, G., Mueller, A., Ruffieux, D., Simeonov, V., and Calpini, B.: Raman Lidar for Meteorological Observations, RALMO – Part 2: Validation of water vapor measurements, *Atmos. Meas. Tech.*, 6, 1347–1358, doi:10.5194/amt-6-1347-2013, 2013. 6581
- Bucholtz, A.: Rayleigh-scattering calculations for the terrestrial atmosphere, *Appl. Optics*, 34, 2765–2773, doi:10.1364/AO.34.002765, 1995. 6574
- Crewell, S. and Löhnert, U.: Accuracy of boundary layer temperature profiles retrieved with multifrequency multiangle microwave radiometry, *IEEE T. Geosci. Remote*, 45, 2195–2201, doi:10.1109/TGRS.2006.888434, 2007. 6572

Water vapour lidar calibration

A. Foth et al.

Title Page

Abstract

Introduction

Conclusions

References

Tables

Figures



Back

Close

Full Screen / Esc

Printer-friendly Version

Interactive Discussion



Water vapour lidar calibration

A. Foth et al.

Title Page

Abstract

Introduction

Conclusions

References

Tables

Figures



Back

Close

Full Screen / Esc

Printer-friendly Version

Interactive Discussion



- Di Girolamo, P., Summa, D., and Ferretti, R.: Multiparameter Raman lidar measurements for the characterization of a dry stratospheric intrusion event, 26, 1742–1762, doi:10.1175/2009JTECHA1253.1, 2009. 6571
- Dionisi, D., Congeduti, F., Liberti, G. L., and Cardillo, F.: Calibration of a multichannel water vapor Raman lidar through noncollocated operational soundings: optimization and characterization of accuracy and variability, *J. Atmos. Ocean. Tech.*, 27, 108, doi:10.1175/2009JTECHA1327.1, 2010. 6576
- England, M. N., Ferrare, R. A., Melfi, S. H., Whiteman, D. N., and Clark, T. A.: Atmospheric water vapor measurements: comparison of microwave radiometry and lidar, *J. Geophys. Res.*, 97, 899–916, doi:10.1029/91JD02384, 1992. 6575
- Ferrare, R. A., Melfi, S. H., Whiteman, D. N., Evans, K. D., Schmidlin, F. J., and Starr, D. O.: A comparison of water vapor measurements made by Raman lidar and radiosondes, *J. Atmos. Oceanic Technol.*, 12, 1177–1195, doi:10.1175/1520-0426(1995)012<1177:ACOWVM>2.0.CO;2, 1995. 6576
- Hartmann, D., Klein Tank, A., Rusticucci, M., Alexander, L., Brönnimann, S., Charabi, Y., Dentener, F., Dlugokencky, E., Easterling, D., Kaplan, A., Soden, B., Thorne, P., Wild, M., and Zhai, P.: Observations: atmosphere and surface, in: *Climate Change 2013: the Physical Science Basis*, contribution of Working Group I to the Fifth Assessment Report of the Intergovernmental Panel on Climate Change, edited by: Stocker, T., Qin, D., Plattner, G., Tignor, M., Allen, S., Boschung, J., Nauels, A., Xia, Y., Bex, V., and Midgley, P., Cambridge University Press, Cambridge, UK and New York, NY, USA, 2013. 6568
- Held, I. and Soden, B.: Water vapor feedback and global warming, *Annu. Rev. Energy. Env.*, 25, 441–475, doi:10.1146/annurev.energy.25.1.441, 2000. 6568
- Herold, C., Althausen, D., Müller, D., Tesche, M., Seifert, P., Engelmann, R., Flamant, C., Bhawar, R., and di Girolamo, P.: Comparison of Raman lidar observations of water vapor with COSMO-DE forecasts during COPS 2007, *Weather Forecast.*, 26, 1056–1066, doi:10.1175/2011WAF2222448.1, 2011. 6569, 6576
- Löhnert, U. and Crewell, S.: Accuracy of cloud liquid water path from ground-based microwave radiometry 1. Dependency on cloud model statistics, *Radio Sci.*, 38, 8041, doi:10.1029/2002RS002654, 2003. 6572
- Macke, A.: HOPE – a German intensive field campaign to capture the spatiotemporal variability of the thermodynamics, energetics, and microphysics of the cloudy troposphere with

Water vapour lidar calibration

A. Foth et al.

Title Page

Abstract

Introduction

Conclusions

References

Tables

Figures



Back

Close

Full Screen / Esc

Printer-friendly Version

Interactive Discussion



high resolution, in: 14th Conference on Atmospheric Radiation, Boston, MA, USA, 7–11 July 2014, J6.4, 2014. 6570

Madonna, F., Amodeo, A., Boselli, A., Cornacchia, C., Cuomo, V., D'Amico, G., Giunta, A.,
Mona, L., and Pappalardo, G.: CIAO: the CNR-IMAA advanced observatory for atmospheric
5 research, *Atmos. Meas. Tech.*, 4, 1191–1208, doi:10.5194/amt-4-1191-2011, 2011. 6569,
6576

Mattis, I., Ansmann, A., Althausen, D., Jaenisch, V., Wandinger, U., Müller, D., Arshinov, Y. F.,
Bobrovnikov, S. M., and Serikov, I. B.: Relative-humidity profiling in the troposphere with
a Raman lidar, *Appl. Optics*, 41, 6451–6462, doi:10.1364/AO.41.006451, 2002. 6569, 6576

10 Mona, L., Cornacchia, C., D'Amico, G., Di Girolamo, P., Pappalardo, G., Pisani, G., Summa, D.,
Wang, X., and Cuomo, V.: Characterization of the variability of the humidity and cloud fields
as observed from a cluster of ground-based lidar systems, *Q. J. Roy. Meteor. Soc.*, 133,
257–271, doi:10.1002/qj.160, 2007. 6578

Müller, D., Ansmann, A., Mattis, I., Tesche, M., Wandinger, U., Althausen, D., and Pisani, G.:
15 Aerosol-type-dependent lidar ratios observed with Raman lidar, *J. Geophys. Res.*, 112,
D16202, doi:10.1029/2006JD008292, 2007. 6574

Nash, J., Smout, R., Oakley, T., Pathack, B., and Kurnosenko, S.: WMO Intercomparison of
High Quality Radiosonde Systems: Final Report, WMO Rep., 118 pp., 2005. 6576

Nash, J., Oakley, T., Vömel, H., and Wei, L.: WMO Intercomparison of High Quality Radiosonde
20 Systems, WMO Rep., 2011. 6572

Navas-Guzmán, F., Fernández-Gálvez, J., Granados-Muñoz, M. J., Guerrero-Rascado, J. L.,
Bravo-Aranda, J. A., and Alados-Arboledas, L.: Tropospheric water vapour and relative hu-
midity profiles from lidar and microwave radiometry, *Atmos. Meas. Tech.*, 7, 1201–1211,
doi:10.5194/amt-7-1201-2014, 2014. 6581

25 Newsom, R. K., Turner, D. D., Mielke, B., Clayton, M., Ferrare, R., and Sivaraman, C.: Simul-
taneous analog and photon counting detection for Raman lidar, *Appl. Opt.*, 48, 3903–3914
doi:10.1364/AO.48.003903, 2009. 6571

Reichardt, J., Wandinger, U., Klein, V., Mattis, I., Hilber, B., and Begbie, R.: RAMSES: German
Meteorological Service autonomous Raman lidar for water vapor, temperature, aerosol, and
cloud measurements, *Appl. Optics*, 51, 8111–8131, doi:10.1364/AO.51.008111, 2012. 6576

30 Rose, T., Crewell, S., Löhnert, U., and Simmer, C.: A network suitable microwave ra-
diometer for operational monitoring of the cloudy atmosphere, *Atmos. Res.*, 75, 183–200,
doi:10.1016/j.atmosres.2004.12.005, 2005. 6572

Water vapour lidar calibration

A. Foth et al.

Title Page

Abstract

Introduction

Conclusions

References

Tables

Figures



Back

Close

Full Screen / Esc

Printer-friendly Version

Interactive Discussion



- Sakai, T., Nagai, T., Nakazato, M., Matsumura, T., Orikasa, N., and Shoji, Y.: Comparisons of Raman Lidar measurements of tropospheric water vapor profiles with radiosondes, hygrometers on the meteorological observation tower, and GPS at Tsukuba, Japan, *J. Atmos. Ocean. Tech.*, 24, 1407–1423, doi:10.1175/JTECH2056.1, 2007. 6578
- 5 Tompkins, A. M.: A prognostic parameterization for the subgrid-scale variability of water vapor and clouds in large-scale models and its use to diagnose cloud cover, *J. Atmos. Sci.*, 59, 1917–1942, doi:10.1175/1520-0469(2002)059<1917:APPFTS>2.0.CO;2, 2002. 6568
- Turner, D. D. and Goldsmith, J. E. M.: Twenty-four-hour Raman lidar water vapor measurements during the atmospheric radiation measurement program's 1996 and 1997 water vapor
10 intensive observation periods, *J. Atmos. Ocean. Tech.*, 16, 1062–1076, doi:10.1175/1520-0426(1999)016<1062:TFHRLW>2.0.CO;2, 1999. 6570, 6576
- Turner, D. D., Ferrare, R. A., Brasseur, L. A. H., Feltz W. F., and Tooman T. P.: Automated retrievals of water vapor and aerosol profiles from an operational raman lidar, *J. Atmos. Ocean. Tech.*, 19, 37–50, doi:10.1175/1520-0426(2002)019<0037:AROWVA>2.0.CO;2, 2002. 6570
- 15 Turner, D. D., Lesht, B. M., Clough, S. A., Liljegren, J. C., Revercomb, H. E., and Tobin, D. C.: Dry bias and variability in vaisala RS80-H radiosondes: the ARM experience, *J. Atmos. Ocean. Tech.*, 20, 117–132, doi:10.1175/1520-0426(2003)020<0117:DBAVIV>2.0.CO;2, 2003. 6576
- Twomey, S.: Aerosols, clouds and radiation, *Atmos. Environ.*, 25, 2435–2442, doi:10.1016/0960-1686(91)90159-5, 1991. 6568
- 20 Wandinger, U.: Raman lidar, in: *Lidar – Range-Resolved Optical Remote Sensing of the Atmosphere*, edited by: Weitkamp, C., vol. 102 of Springer Series in Optical Sciences, Springer Berlin, Heidelberg, 241–271, 2005. 6569, 6573
- Weckwerth, T. M., Parsons, D. B., Koch, S. E., Moore, J. A., Lemone, M. A., Demoz, B. B., Flamant, C., Geerts, B., Wang, J., and Feltz, W. F.: An overview of the international H₂O project (IHOP_2002) and some preliminary highlights, *B. Am. Meteorol. Soc.*, 85, 253–277, doi:10.1175/BAMS-85-2-253, 2004. 6569
- 25 Westwater, E. R., Crewell, S., Mätzler, C., and Cimini, D.: Principles of surface-based microwave and millimeter wave radiometric remote sensing of the troposphere, *Quad. Soc. Ital. Elettromagnetismo*, 1, 50–90, 2005. 6569
- 30 Whiteman, D. N.: Examination of the traditional Raman lidar technique. II. Evaluating the ratios for water vapor and aerosols, *Appl. Optics*, 42, 2593–2608, doi:10.1364/AO.42.002593, 2003. 6573, 6575

Water vapour lidar calibration

A. Foth et al.

Title Page

Abstract

Introduction

Conclusions

References

Tables

Figures



Back

Close

Full Screen / Esc

Printer-friendly Version

Interactive Discussion



Whiteman, D. N., Melfi, S. H., and Ferrare, R. A.: Raman lidar system for the measurement of water vapor and aerosols in the earth's atmosphere, *Appl. Optics*, 31, 3068–3082, doi:10.1364/AO.31.003068, 1992. 6569

Whiteman, D. N., Demoz, B., di Girolamo, P., Comer, J., Veselovskii, I., Evans, K., Wang, Z., Cadirola, M., Rush, K., Schwemmer, G., Gentry, B., Melfi, S. H., Mielke, B., Venable, D., and van Hove, T.: Raman lidar measurements during the international H₂O project. Part I: Instrumentation and analysis techniques, *J. Atmos. Ocean. Tech.*, 23, 157–169, doi:10.1175/JTECH1838.1, 2006a. 6571

Whiteman, D. N., Demoz, B., di Girolamo, P., Comer, J., Veselovskii, I., Evans, K., Wang, Z., Sabatino, D., Schwemmer, G., Gentry, B., Lin, R.-F., Behrendt, A., Wulfmeyer, V., Browell, E., Ferrare, R., Ismail, S., and Wang, J.: Raman lidar measurements during the international H₂O project. Part II: Case studies, *J. Atmos. Ocean. Tech.*, 23, 170–183, doi:10.1175/JTECH1839.1, 2006b. 6569

Wulfmeyer, V., Behrendt, A., Kottmeier, C., Corsmeier, U., Barthlott, C., Craig, G. C., Hagen, M., Althausen, D., Aoshima, F., Arpagaus, M., Bauer, H.-S., Bennett, L., Blyth, A., Brandau, C., Champollion, C., Crewell, S., Dick, G., di Girolamo, P., Dorninger, M., Dufournet, Y., Eigenmann, R., Engelmann, R., Flamant, C., Foken, T., Gorgas, T., Grzeschik, M., Handwerker, J., Hauck, C., Höller, H., Junkermann, W., Kalthoff, N., Kiemle, C., Klink, S., König, M., Krauss, L., Long, C. N., Madonna, F., Mobbs, S., Neining, B., Pal, S., Peters, G., Pigeon, G., Richard, E., Rotach, M. W., Russchenberg, H., Schwitalla, T., Smith, V., Steinacker, R., Trentmann, J., Turner, D. D., van Baelen, J., Vogt, S., Volkert, H., Weckwerth, T., Wernli, H., Wieser, A., and Wirth, M.: The Convective and Orographically-induced Precipitation Study (COPS): the scientific strategy, the field phase, and research highlights, *Q. J. Roy. Meteor. Soc.*, 137, 3–30, doi:10.1002/qj.752, 2011. 6569

Water vapour lidar calibration

A. Foth et al.

Title Page

Abstract

Introduction

Conclusions

References

Tables

Figures



Back

Close

Full Screen / Esc

Printer-friendly Version

Interactive Discussion

**Table 1.** Calibration factors and errors of the regression, profile and IWV method.

Method	$C_{\text{H}_2\text{O}}$ (g kg^{-1})	$\sigma C_{\text{H}_2\text{O}}$ (g kg^{-1})
Regression	12.15	0.21
Profile	12.55	1.12
IWV	12.78	0.3

Water vapour lidar calibration

A. Foth et al.

Title Page

Abstract

Introduction

Conclusions

References

Tables

Figures



Back

Close

Full Screen / Esc

Printer-friendly Version

Interactive Discussion

**Table 2.** Absolute and relative bias for water vapour mixing ratio (mean \pm SD). Values are represented for the layers from 0 to 2 km, from 2 to 4 km and from 4 to 10 km.

	0–2 km		2–4 km		4–10 km	
	Abs. bias (g kg ⁻¹)	Rel. bias (%)	Abs. bias (g kg ⁻¹)	Rel. bias (%)	Abs. bias (g kg ⁻¹)	Rel. bias (%)
RS-Polly ^{XT}	-0.04 \pm 0.17	-1.11 \pm 3.25	0.12 \pm 0.11	6.26 \pm 5.09	0 \pm 0.03	3.18 \pm 15.5
RS-BASIL	-0.2 \pm 0.4	-5.34 \pm 8.17	-0.15 \pm 0.11	-7.16 \pm 5.07	0.01 \pm 0.04	0.87 \pm 26.49
Polly ^{XT} -BASIL	-0.3 \pm 0.3	-6.67 \pm 6.59	-0.13 \pm 0.08	-7.69 \pm 2.95	-0.02 \pm 0.04	15.39 \pm 148.5

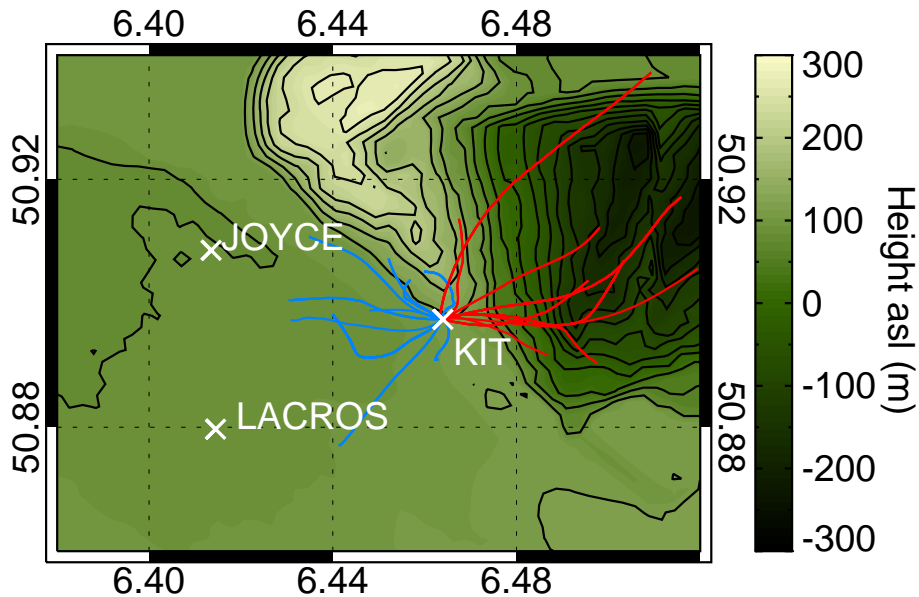


Figure 1. Map of the area around Jülich with westward (blue) and eastward (red) RS trajectories. The darker area in the east indicates the open-cast mining and the brighter area in the north indicates a hill named Sophienhöhe.

Water vapour lidar calibration

A. Foth et al.

Title Page	
Abstract	Introduction
Conclusions	References
Tables	Figures
◀	▶
◀	▶
Back	Close
Full Screen / Esc	
Printer-friendly Version	
Interactive Discussion	



Water vapour lidar calibration

A. Foth et al.

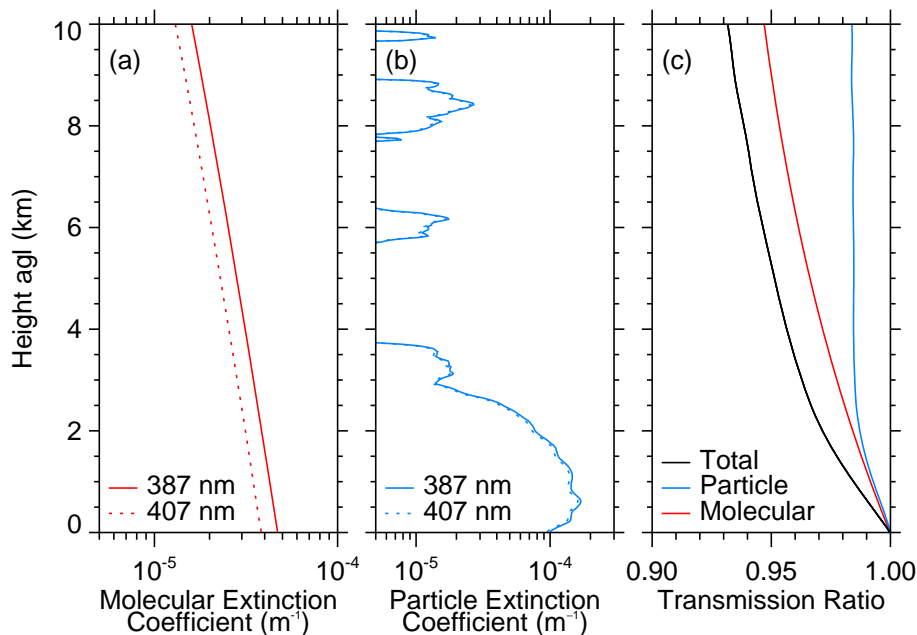


Figure 2. (a) Calculated profiles of the molecular extinction coefficient at 387 and 407 nm. (b) Determined particle extinction coefficient at 387 and 407 nm from a Polly^{XT} measurement on 5 May 2013, 23:10 UTC. (c) Resulting transmission ratio considering the molecular (red), the particle (blue) contribution and the the sum of both (black).

[Title Page](#)[Abstract](#)[Introduction](#)[Conclusions](#)[References](#)[Tables](#)[Figures](#)[◀](#)[▶](#)[◀](#)[▶](#)[Back](#)[Close](#)[Full Screen / Esc](#)[Printer-friendly Version](#)[Interactive Discussion](#)

Water vapour lidar calibration

A. Foth et al.

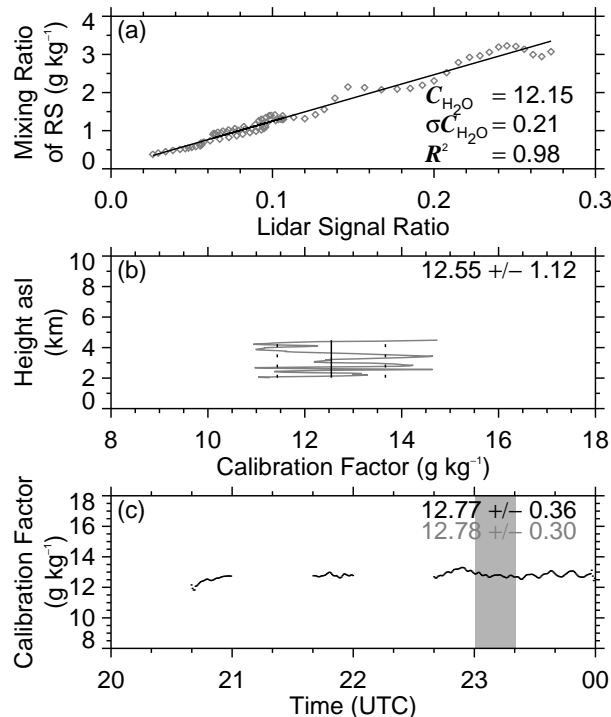


Figure 3. Calibration methods for a clear sky night from a Polly^{XT} measurement on 5 May 2013 (HOPE IOP 12): **(a)** regression method. Water vapour mixing ratio of the radiosonde (RS) as function of the signal ratio from the lidar averaged over 20 min from 23:00 to 23:20 UTC. $C_{\text{H}_2\text{O}}$ is the slope of the regression line, $\sigma_{C_{\text{H}_2\text{O}}}$ is the standard error of the slope and R^2 is the coefficient of determination. **(b)** Profile method. The calibration factor for each considered height bin. The numbers indicate the mean calibration factor and its standard deviation. **(c)** IWV method. Time series of the calculated calibration factor (black line). The black numbers denote the mean and the standard deviation of the whole time range, whereas the grey numbers correspond to the time range of the RS ascent (grey area).

Water vapour lidar
calibration

A. Foth et al.

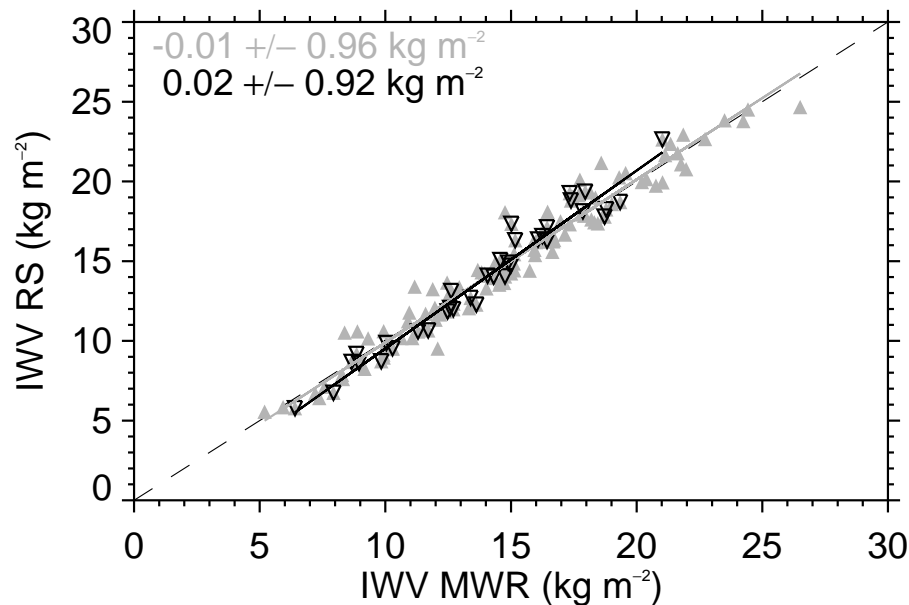


Figure 4. Comparison between IWV from MWR and RS. Grey and black triangles indicate all weather conditions and only clear sky conditions, respectively. The solid lines notify the according regression lines. The numbers in the upper left corners denote the bias and the standard deviation, respectively.

[Title Page](#)[Abstract](#)[Introduction](#)[Conclusions](#)[References](#)[Tables](#)[Figures](#)[◀](#)[▶](#)[◀](#)[▶](#)[Back](#)[Close](#)[Full Screen / Esc](#)[Printer-friendly Version](#)[Interactive Discussion](#)

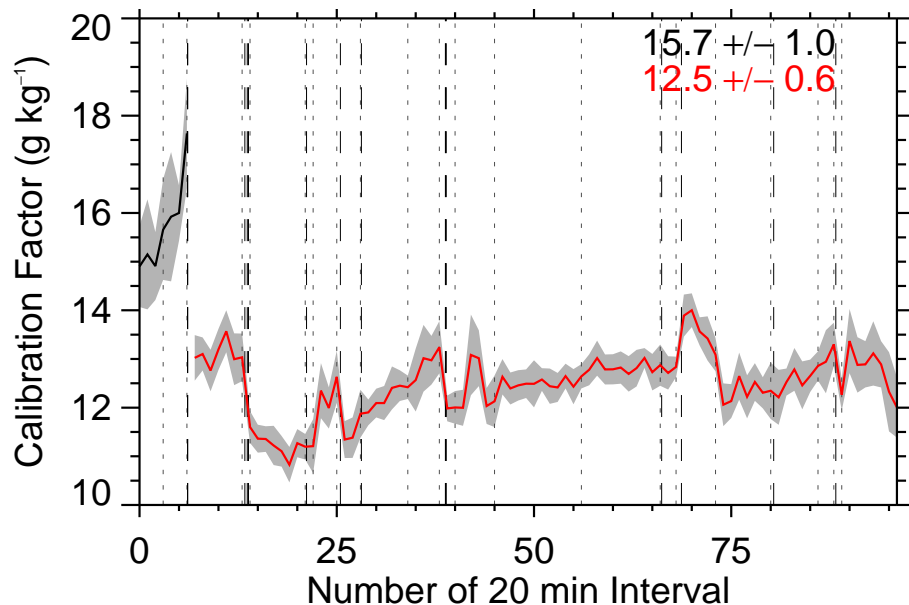


Figure 5. Calibration factor of Polly^{XT} using the IWV method as function of time given in number of 20 min interval. The black and the red solid lines indicate the calibration factor before and after the rearrangement of the optical setup on 15 April 2013, 10:06 UTC, respectively. The grey areas denote the standard deviation during each 20 min interval. The numbers on the top represent the according means and standard deviations over the time. The grey dashed lines demonstrate rearrangements on Polly^{XT} especially adjustments of the overlap or cleanups of the quartz plate in the roof of the Polly^{XT} cabinet. The grey dotted lines indicate leaps in the time of more than 4 h.

Title Page

Abstract

Introduction

Conclusions

References

Tables

Figures

◀

▶

◀

▶

Back

Close

Full Screen / Esc

Printer-friendly Version

Interactive Discussion



Water vapour lidar calibration

A. Foth et al.

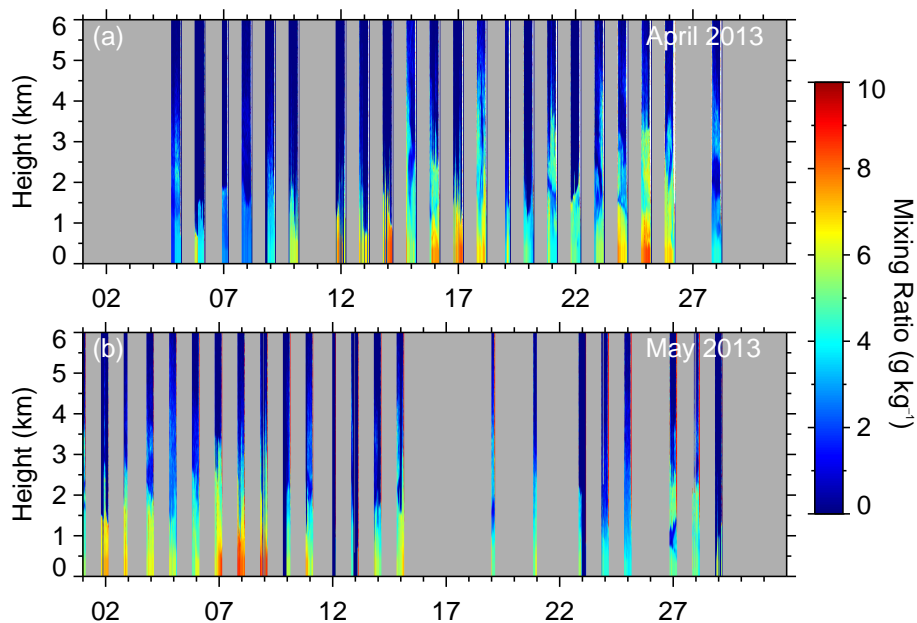


Figure 6. Overview over the water vapour profiles observed by Polly^{XT} during HOPE: (a) April and (b) May 2013.

[Title Page](#)[Abstract](#)[Introduction](#)[Conclusions](#)[References](#)[Tables](#)[Figures](#)[◀](#)[▶](#)[◀](#)[▶](#)[Back](#)[Close](#)[Full Screen / Esc](#)[Printer-friendly Version](#)[Interactive Discussion](#)

Water vapour lidar
calibration

A. Foth et al.

Title Page

Abstract

Introduction

Conclusions

References

Tables

Figures

◀

▶

◀

▶

Back

Close

Full Screen / Esc

Printer-friendly Version

Interactive Discussion

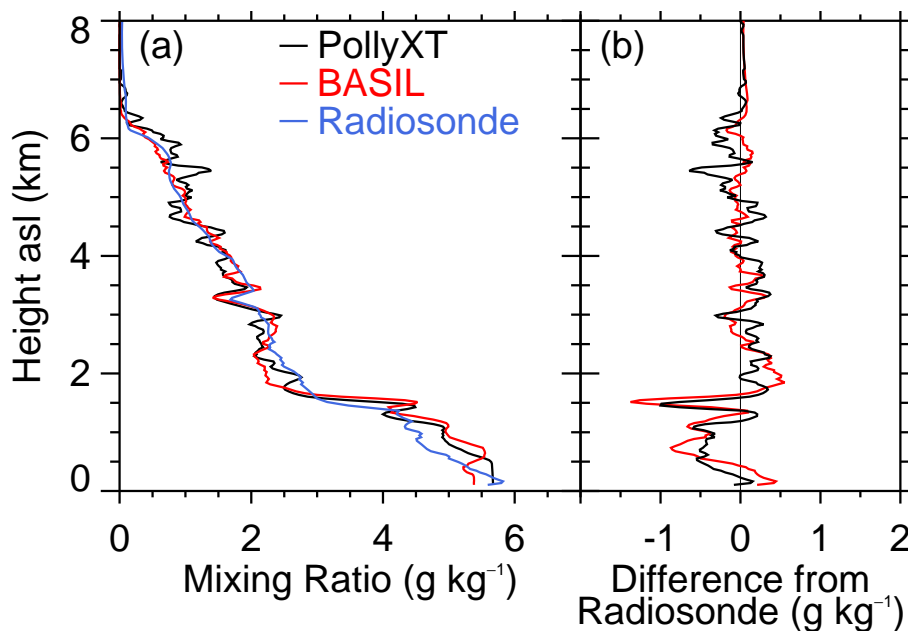


Figure 7. (a) Comparison of the mixing ratio profiles from Polly^{XT} (black), BASIL (red) and radiosonde (blue) on 5 May 2013, 23:00 UTC. (b) Differences in mixing ratio between radiosonde and Polly^{XT} or BASIL, respectively.

Water vapour lidar
calibration

A. Foth et al.

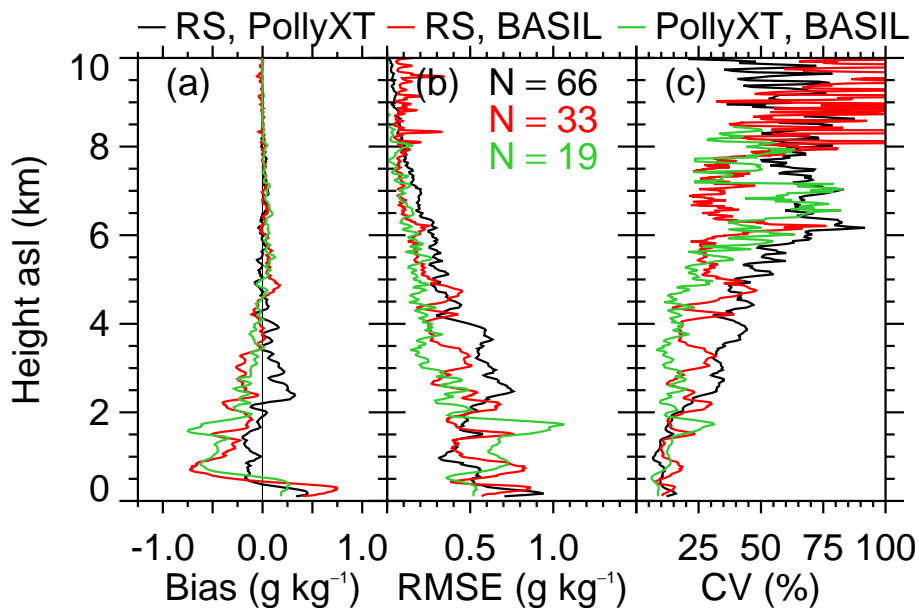


Figure 8. (a) Absolute bias between the radiosonde (RS) and Polly^{XT} (black), between RS and BASIL (red) and between Polly^{XT} and BASIL (green). (b) Root-mean-square error (RMSE) of the water vapour mixing ratio. The numbers indicate the sample size. (c) Coefficient of variation (CV, relative RMSE).

Title Page

Abstract

Introduction

Conclusions

References

Tables

Figures

◀

▶

◀

▶

Back

Close

Full Screen / Esc

Printer-friendly Version

Interactive Discussion



Water vapour lidar
calibration

A. Foth et al.

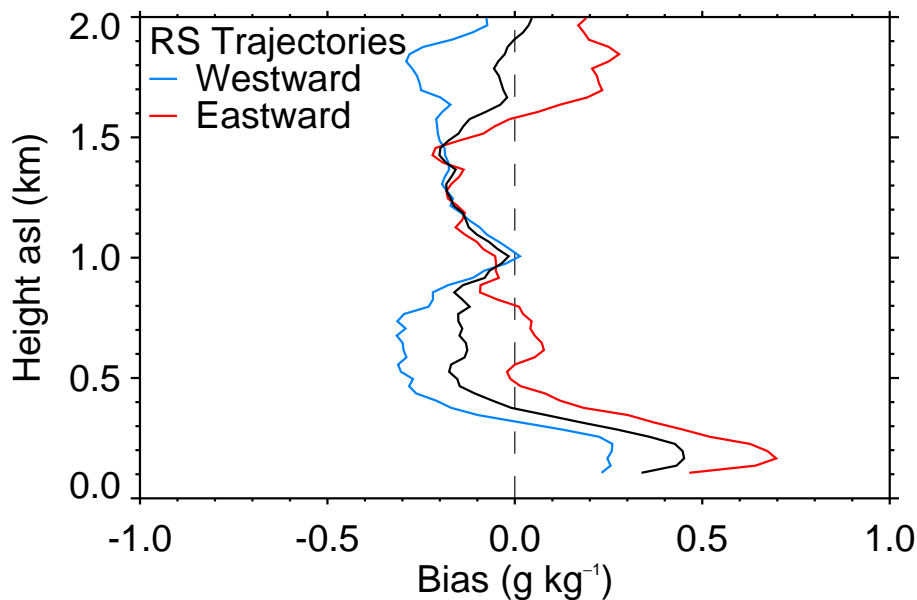


Figure 9. Absolute bias between the RS and Polly^{XT} distinguished by different trajectories. The black line indicates the bias considering all trajectories.

[Title Page](#)[Abstract](#)[Introduction](#)[Conclusions](#)[References](#)[Tables](#)[Figures](#)[◀](#)[▶](#)[◀](#)[▶](#)[Back](#)[Close](#)[Full Screen / Esc](#)[Printer-friendly Version](#)[Interactive Discussion](#)

Water vapour lidar calibration

A. Foth et al.

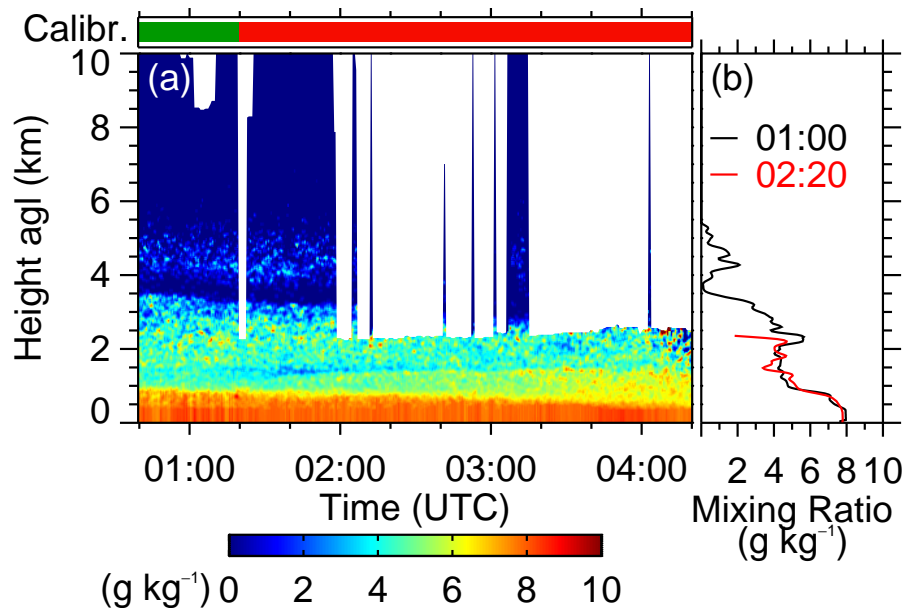


Figure 10. (a) Height-time display of the water vapour mixing ratio from a Polly^{XT} measurement on 16 April 2013, 00:40 UTC. White areas are regions in or above clouds without any water vapour information. The bars on the top indicate which profiles are calibrated (green) based on the current IWV from MWR. The red bars denote profiles which are calibrated with the averaged calibration factor from the last clear sky 20 min interval (red). (b) Profiles of the 20 min intervals at 01:00 UTC (black) and 02:20 UTC (red).

Title Page

Abstract

Introduction

Conclusions

References

Tables

Figures

◀

▶

◀

▶

Back

Close

Full Screen / Esc

Printer-friendly Version

Interactive Discussion

